Int J Adv Manuf Technol (2015) 79:101–111
DOI 10.1007/s00170-015-6789-8

ORIGINAL ARTICLE

Laser cutting of small diameter hole in aluminum foam

B. S. Yilbas · S. S. Akhtar · O. Keles

Received: 3 April 2012 / Accepted: 5 January 2015 / Published online: 30 January 2015

Abstract Laser cutting of a small diameter hole into aluminum foam is carried out, and thermal stress field developed in the cutting section is examined incorporating the finite element code. Laser cutting experiments are conducted to examine the morphological changes in the cut sections through using scanning electron microscope, energy-dispersive spectroscopy, and X-ray diffraction. It is found that von Mises stress attains high values in the region where the temperature gradient is high. The slow cooling of the last cut region in the hole circumference suppresses the stress level in this region. Holes cut are parallel sided and free from defects such as sideway burning and large burr formation.

Keywords Laser · Cutting · Aluminum foam · Thermal stress

1 Introduction

Aluminum foam finds wide applications in thermal plants due to its high thermal performance and light weight structure. Machining of the foam material is difficult due to the applied mechanical cutting force, which may result in failure of the machined sections through buckling, collapse, and fracture. One of the methods for machining of aluminum foams is to use a laser beam source without applying a mechanical force. In addition, laser machining provides advantages over the conventional machining processes including precision of operation, low-cost fast processing, and nonmechanical contact. However, during laser machining, thermal effects result in stress levels in the machined regions, which limit the practical applications of the parts being machined. The stress levels become important, due to presence of high-temperature gradients, for cutting of the small diameter holes. Consequently, investigation into laser cutting of small diameter holes into aluminum foam and resulting thermal stress field around the cut section becomes necessary.

Considerable research studies were carried out to examine processing of metallic foams. The review on laser machining applications including the cutting process was carried out by Latham and Kar [1] and Dubey and Yadava [2]. They presented the importance and advantages of the laser machining process. The recent progresses in high-power fiber laser machining applications were presented by Carter and Li [3]. They discussed the effective use of high-power fiber lasers in precision machining applications. Laser machining of magnesium foams and thermal analysis was carried out by Murakami et al. [4]. They used lotus-type porous elements in the analysis and indicated that findings agreed well with the experimental data. Laser bending of aluminum foams was investigated by Guglielmotti et al. [5]. Their findings revealed that the collapse of the cellular structures did not take place; however, many laser scan tracks were required to obtain sufficient bending angles. Laser-assisted aluminum foaming was studied by Kathuria et al. [6]. They suggested that a pore size and density gradients existed in the structure as the laser processing parameters were changed. Fabrication and characteristics of thermoplastic microsphere nanocomposite foams were investigated by Rangari et al. [7]. They indicated that a significant increase in compressive strength and modulus of elasticity occurred for nanocomposite foam samples as compared to the neat foam samples. Manufacturing of metal foam layers by laser metal deposition technique was investigated by Carcel et al. [8]. They showed that the laser beam could be

B. S. Yilbas (✉) · S. S. Akhtar
ME Department, King Fahd University of Petroleum and Minerals, Dhahran, Saudi Arabia
e-mail: bsyilbas@kfupm.edu.sa

O. Keles
ME Department, Gazi University, Ankara, Turkey

used effectively to produce high-porosity foam coatings. Laser interaction with low-density carbon foam was studied by Chaurasia et al. [9]. They demonstrated that the foam targets smoothed the crater formed by the laser irradiation. Laser hole drilling in foam samples was examined by Yoshida et al. [10]. They indicated that the laser processing was suitable for machining of foam material, particularly for drilling process. Laser machining of foam substrates using Nd/YAG laser was carried out by Fujimura et al. [11]. They incorporated thermal characteristics and absorption spectrum of the foam to optimize the cutting conditions.

Although laser cutting of small hole diameter in titanium alloy was studied previously [12], the thermal response of the foam structure including the thermal stresses was not investigated before. In addition, the formulation of the thermal stress field for a solid metallic substrate and the foam material differs significantly during laser cutting due to the presence of large voids in the foam material. Consequently, in the present study, laser cutting of 4-mm diameter holes into aluminum foam plates is carried out. Temperature and stress fields developed are simulated during and after the cutting process using ABAQUS finite element code. The cutting sections are characterized using SEM, EDS, and XRD.

2 Mathematical modeling

Figure 1 shows the schematic view of the laser cutting of small diameter hole and the coordinate system. Since aluminum foam consists of pore cells, the governing equation of energy transfer for cutting needs to be modified to incorporate the presence of pores in the workpiece. In this case, the continuum conservation equations are used in the simulations with the assumption of effective properties resembling aluminum foam workpiece properties. The similar approach is also incorporated in the previous studies [4, 13]. The Fourier heat transfer equation pertinent to the laser heating process can be written as

$$\rho_{eff}\frac{\partial H(T)}{\partial t} = \left(\nabla\left(k_{eff}(T)\nabla T\right)\right) + S_o \tag{1}$$

where ρ_{eff} is the effective density, H is the temperature-dependent enthalpy including the latent heat of solidification, k_{eff} is the temperature-dependent thermal conductivity, and S_o is the heat source term resembling the laser beam, i.e.,

$$S_o = I_o e^{-\delta z}\left(1-r_f\right)e^{\left(-\frac{(x-rSinwt)^2+(y-rCoswt)^2}{a^2}\right)} \tag{2}$$

I_o is the laser power peak density, a is the Gaussian parameter, r_f is the surface reflectivity, δ is the absorption coefficient, ρ is the density, and x and y are the axes while the laser beam scans the surface along the circumference of the cut hole, then, $r = \sqrt{x^2+y^2}$, i.e., the circular cutting is carried out and the laser beam motion follows the circumference of the laser cut hole with a constant angular speed ω. The absorption coefficient of the laser beam (δ) after the key hole formation is considered, i.e.:

$$\delta = \frac{1}{L}\ln\left(\frac{I_o}{I_L}\right) \tag{3}$$

where L is the thickness of the workpiece, I_o is the peak power intensity at the workpiece surface, I_L is the laser power

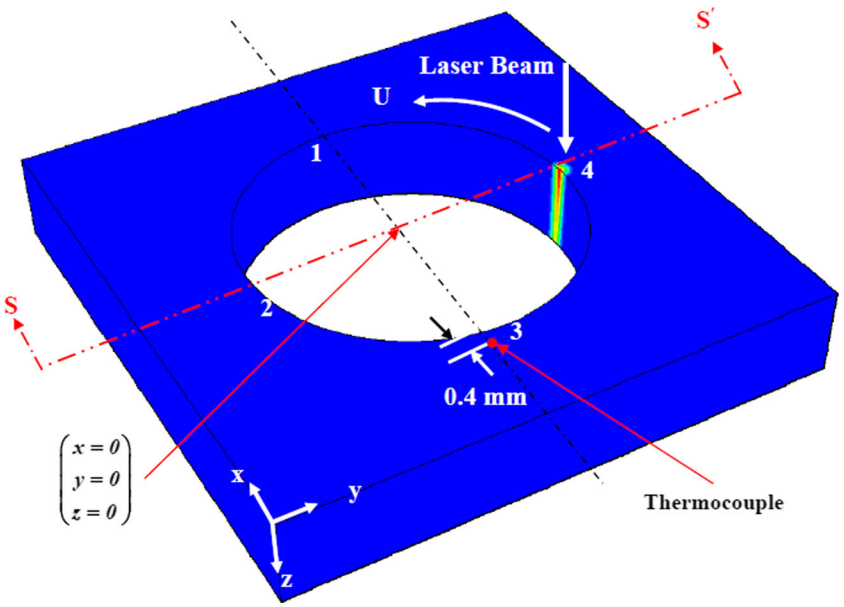

Fig. 1 A schematic view of laser circular cutting and location of points around the hole circumference

intensity at the workpiece thickness. The laser beam axis is parallel to the *z*-axis (Fig. 1). It should be noted that the laser beam intensity distribution is assumed to be Gaussian at the irradiated surface.

The thermal analysis is conducted incorporating temperature-dependent material properties. The values of density, specific heat, and thermal conductivity are determined from the equivalent properties of the lotus-type aluminum porous metal. The effective density of aluminum foam is 250 kg/m^3. The equivalent properties of the lotus-type porous metal can be expressed through the following equations [4]:

$$\rho_{eff}(T) = (1-\varepsilon)\rho_s(T) + \varepsilon\rho_f(T) \tag{4}$$

and

$$C_{peff}(T) = \frac{(1-\varepsilon)\rho_s(T)C_{ps}(T) + \varepsilon\rho_f(T)C_{pf}(T)}{(1-\varepsilon)\rho_s(T) + \rho_f(T)} \tag{5}$$

and

$$k_{eff}(T) = \frac{(1-\varepsilon)\rho_s(T)k_s(T) + \varepsilon\rho_f(T)k_f(T)}{(1-\varepsilon)\rho_s(T) + \varepsilon\rho_f(T)} \tag{6}$$

where $\rho_{sub}(T)$, $C_{psub}(T)$, and $k_{eff}(T)$ are the density and specific heat of porous metal, respectively, and ε is the porosity expressed by the volume ratio of pores versus the total volume of the porous metal. The subscripts (sub) "*eff*," "*s*," and "*f*" indicate the effective property, property of the nonporous aluminum metal, and property of the gas in the pores, respectively. The effective properties are given in Table 1.

Table 1 Properties of aluminum foam used in the simulations

Temperature (K)	Effective specific heat (J/kg K)	Effective thermal conductivity (W/m K)	Yield stress (MPa)
300	870	9.07	1.0
400	920	9.16	0.8
500	970	9.09	0.65
600	1000	9.15	0.49
700	1030	9.69	0.26
800	1050	9.93	0.24
823	1050	9.93	0.12
893	1050	9.93	0.015

Effective density (ρ_{eff})=250 kg/m^3: latent heat=370,000 J/kg: solidus temperature=835 K: liquidus temperature=865 K. Expansion coefficient=2.34×10^{-5} 1/K: Poisson's ratio=0.02: *crushable foam properties:* compression yield stress ratio=1, plastic Poission's ratio=0.25

The convective and radiation boundary conditions are considered at the free surface of the workpiece. Therefore, the corresponding boundary condition is as follows:

At the irradiated surface (top surface),

$$\frac{\partial T}{\partial z} = \frac{h_f}{k_{eff}}(T_s - T_{amb}) + \frac{\varepsilon_\lambda \sigma}{k_{eff}}\left(T_s^4 - T_{amb}^4\right) \tag{7}$$

where h_f (=3000 W/m^{2}K [14]) is the forced convection heat transfer coefficient due to the assisting gas and ε_λ is the emissivity of the surface.

At the bottom surface

$$\frac{\partial T}{\partial y} = \frac{h}{k_{eff}}(T_s - T_{amb}) + \frac{\varepsilon_\lambda \sigma}{k_{eff}}\left(T_s^4 - T_{amb}^4\right): \frac{\partial T}{\partial z} = \frac{h}{k_{eff}}(T_s - T_{amb}) + \frac{\varepsilon_\lambda \sigma}{k_{eff}}\left(T_s^4 - T_{amb}^4\right) \tag{8}$$

where h (=20 W/m^{2}K) is the heat transfer coefficient due to natural convection, and T_s and T_{amb} are the surface and ambient temperatures, respectively, ε is the emissivity (ε_λ=0.9 is considered), σ is the Stefan-Boltzmann constant (σ=5.67×10^{-8} W/m^{2}K^4). At far away boundary (at edges of the solution domain), constant temperature boundary is assumed (T=293 K), i.e.,

$$x = \infty \;\; ; \;\; y = \infty \;\; ; \;\; z = t_h \;\; \rightarrow \;\; \mathrm{T} \;=\; 293\ \mathrm{K} \tag{9}$$

where t_h is the thickness of the workpiece (t_h=0.008 m). Initially (prior to laser cutting), the substrate material is assumed to be at constant ambient temperature, i.e., $T=T_{amb}$, which is considered as constant (T_{amb}=293 K).

To analyze the phase change problem, the enthalpy method is used [15]. The specific heat capacity is associated with the internal energy gain of the substrate material, i. e., $Cp(T) = \frac{\partial U}{\partial T}$. Latent heat effects are significant in the laser melting of aluminum foam material due to phase change and must be taken into account. The equivalent latent heat ($L_{eq} = \frac{L_s}{1+\frac{\rho_f}{\rho_s}\epsilon\left(1+\frac{\epsilon}{\epsilon-1}\right)}$, where L_{eq} is the equivalent latent heat of melting and L_s is the latent heat of aluminum) is used in terms of solidus and liquidus temperatures (the lower and upper temperature bounds of the phase change range), and the total internal energy associated with the phase change.

Since the primary interest is the stress field developed in the laser-irradiated section, the flow field generated in the liquid phase in the surface vicinity during the laser melting process is omitted. It should be noted that the thermal stress field is considered to be almost zero in the melt pool, since only negligibly small hydrodynamic pressures are present in the melt pool. Since metal foam behavior is different from that of solid metal, classical plastic theory cannot be used to describe

their behaviors. Moreover, classical foundation models such as the Pasternak and the Reissner models have been recently reformulated within the framework of nonlocal mechanics via using the gradient theory of elasticity [16–18]. In this case, a two-dimensional foundation model was introduced through using a mechanically based nonlocal elasticity theory, and the foundation was thought of as an ensemble of soil column elements resting on an elastic base. It was assumed that each column element was acted upon by a local Winkler-like reaction force exerted by the elastic base, contact shear forces, and volume forces to adjacent and nonadjacent column elements. Since the volume contraction of voids in the aluminum foam is simliar to that reported in the open literature [19], the model developed by Deshpande and Fleck [19] is used. The model study is primarily based on the experimental tests of aluminum foam, which has been built in the finite element package ABAQUS [15]. The model assumes isotropic hardening under tension and compression. In the present work, three-dimensional finite element analysis is carried out using the dynamic explicit code ABAQUS/Explicit using the crushable foam model with isotropic hardening. The stress analysis is coupled with the previous thermal analysis to import the thermal history during the laser treatment process. The crushable foam plasticity model available in ABAQUS is based on the assumption that the resulting deformation is not recoverable instantaneously and it can be idealized as plastic for short duration events. The contribution of the mean stress on the yield function is realized through a material parameter known as a shape factor. It defines the aspect ratio of the elliptical stress. The shape factor quantitatively distinguishes the plastic behavior of metal foams from solid metals. The yield function (F) is given by [19]

$$F = \sqrt{q^2 + \alpha^2 p^2} - B = 0 \tag{10}$$

where q is the von Mises equivalent stress and p is the mean stress. B defines the size of the yield ellipse.

Where

$$q = \sqrt{\frac{3}{2}\mathbf{S}:\mathbf{S}} \quad : \quad p = -\frac{1}{3} trace\,\boldsymbol{\sigma} = -\frac{1}{3}\boldsymbol{\sigma}:\mathbf{I} \quad : \quad B = \alpha p_c = \sigma_c\sqrt{1+\left(\frac{\alpha}{3}\right)^2}$$
$$\alpha = \frac{3k}{\sqrt{9-k^2}} \quad : \quad k = \frac{\sigma_c^o}{p_c^o}$$

where α represents the shape of the yield ellipse in the p–q stress plane, B defines the size of the yield ellipse, p_c is the yield strength in hydrostatic compression, and σ_c is the absolute value of the yield strength in uniaxial compression. The yield surface is the Mises circle in the deviatoric stress plane and an ellipse in the meridional plane. The shape factor, α, remains constant during the process of any plastic deformation. The evolution of the yield ellipse is controlled by an equivalent plastic strain, $\overline{\varepsilon}^{pl}$. In the present study, the compression yield stress ratio k is taken as unity for simplicity.

The flow potential for the isotropic hardening model is chosen as [19]

$$G = \sqrt{q^2 + \beta^2 p^2} \tag{11}$$

where β represents the shape of the flow potential in the p–q stress plane and is related to the plastic Poisson's ratio, ν_p, by

$$\beta = \frac{3}{\sqrt{2}}\sqrt{\frac{1-1\nu_p}{1+\upsilon_p}} \tag{12}$$

The plastic Poisson's ratio, ν_p, which is the ratio of the transverse to the longitudinal plastic strain under uniaxial compression, is defined through the user-defined function and it is considered to be in the range of −1 to 0.5. The upper limit, ν_p,=0.5, corresponds to an incompressible plastic flow. In the current simulation, the value of plastic Poisson's ratio is assumed to be 0.25.

The plastic strains are defined to be normal to a family of self-similar flow potentials parameterized by the value of the potential G [19]:

$$\varepsilon^{pl} = \lambda\frac{\partial G}{\partial \sigma} \tag{13}$$

where λ. is the nonnegative plastic flow multiplier. The hardening of the foam is described through

$$\sigma_c = \sigma_c\left(\overline{\varepsilon}^{pl}\right) \tag{14}$$

where $\overline{\varepsilon}^{pl}$ is the equivalent plastic strain. The evolution of $\overline{\varepsilon}^{pl}$ is assumed to be governed by the equivalent plastic work expression, i.e.,

$$\sigma_c\varepsilon^{pl} = \boldsymbol{\sigma} : \varepsilon^{pl} \tag{15}$$

The equivalent plastic strain is equal to the absolute value of the axial plastic strain in uniaxial tension or compression. The plastic flow is associative when the value of β is the same as that of α. In general, the plastic flow is nonassociated to allow for the independent calibrations of the shape of the yield surface and the plastic Poisson's ratio.

Thermal strains arise due to volume changes caused by both temperature differences and phase

Table 2 Laser cutting conditions used in the experiment

Cutting speed (cm/s) (mm/min)	Angular speed (rad/s)	Power (W)	Frequency (Hz)	Nozzle gap (mm)	Nozzle diameter (mm)	Focus setting (mm)	N_2 pressure (kPa)
15	37.5	2000	1000	1.5	1.5	127	600

transformations, including solidification and solid-state phase changes, i.e.,

$$(\varepsilon_{th})_{ij} = \int_{T_O}^{T} \alpha(T) dT \delta_{ij} \tag{16}$$

where α is the temperature-dependent coefficient of thermal expansion and T_o is the reference temperature which is considered to be 300 K and δ_{ij} is Kronecker's delta.

During the laser cutting process, self-annealing takes place in the previously cut sections due to heat transfer from the irradiated spot. In order to simulate this situation, the consideration is made such that the relaxation of stresses and plastic strains occur as the workpiece is heated to above melting temperature during laser heating and then cooling to room temperature. In this case, temperature-dependent foam hardening suboption in ABAQUS [15] is used during the simulations, and low values of yield stress are assumed above the melting temperature. The temperature-dependent properties used in the simulations are given in Table 1.

3 Experimental

A CO_2 laser (LC-ALPHAIII) delivering nominal output power of 2 kW was used to irradiate the workpiece surface. The power intensity distribution across the irradiated spot is Guassian, which in turn results in the peak power intensity of 3.2×10^{10} W/m^2 at the irradiated spot center and 1.177×10^{10} W/m^2 at $r=a$, a being the Gaussian parameter. The nominal focal length of the focusing lens was 127 mm. The laser beam diameter focused at the workpiece surface was 0.25 mm. Nitrogen-assisting gas emerging from the conical nozzle and coaxially with the laser beam was used. The optimization study for laser cutting parameters was considered. In this case, the cutting tests were repeated to identify the best cutting parameters resulting in less sideway burning around the kerf edges, small dross attachment at the kerf exit, and low striations at the kerf surface. It should be noted that increasing laser output power and lowering laser cutting speed increased the sideway burning and dross attachment at the kerf surface.

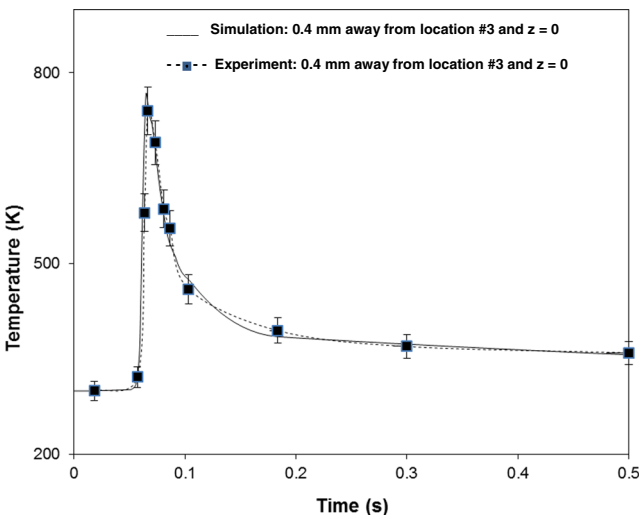

Fig. 2 Temporal variation of temperature predicted from the simulations and obtained from the thermoucouple data

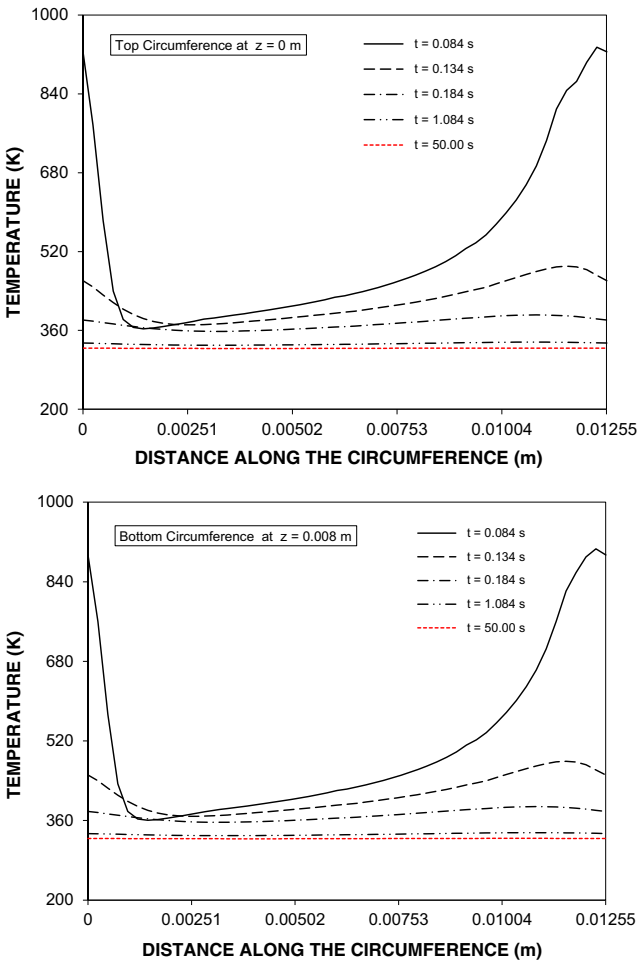

Fig. 3 Temperature variation along hole top and bottom circumferences for different cooling periods

On the other hand, reducing laser output power and increasing laser cutting speed caused incomplete cutting. Therefore, cutting parameters leading to the optimum cutting conditions were selected, which are given in Table 2.

Aluminum foam plates with 8-mm thickness were used as workpieces. Aluminum foam consists of about 89 % Al and 11 % SiO_2 as a foaming agent. JEOL JDX-3530 scanning electron microscope (SEM) is used to obtain photomicrographs of the cross section of the workpieces after the tests. EDS analysis was carried out for three different locations at the kerf surface. The error related to the EDS analysis is estimated based on the repeatability of the data, which is on the order of 3 %. The Bruker D8 Advance having CuKα radiation is used for XRD analysis. A typical setting of XRD was 40 kV and 30 mA.

To validate temperature predictions, the thermocouple was used to monitor the temporal variation of surface temperature at the locations 0.4 mm away from the location no. 3 at cut edge surface (Fig. 1). This was necessary to avoid the melting of the surface of the thermocouples during the laser cutting process. The thermocouple used was K-type, and the end of the thermocouple wires was twisted once prior to attachment. It should be noted that laser pulses with a Guassian beam profile and peak intensities 0.2×10^9 W/m^2 were used in the experiment. Nd/YAG laser was used to attach the thermocouple tips to the surface, since solder would melt at around 200 °C. The response time of the thermocouple was on the order of microseconds, and it was calibrated through comparison of the pyrometer data using a large area constant temperature heat source which could be adjusted to various values of constant temperatures [20]. The experimental error was determined using the experimental repeatability; therefore, the experiments were repeated five times, and the error was estimated in the order of 5 %.

4 Results and discussion

Laser cutting of 4-mm diameter hole into aluminum foam is carried out, and thermal stress field developed around the cut section is investigated by incorporating the ABAQUS code.

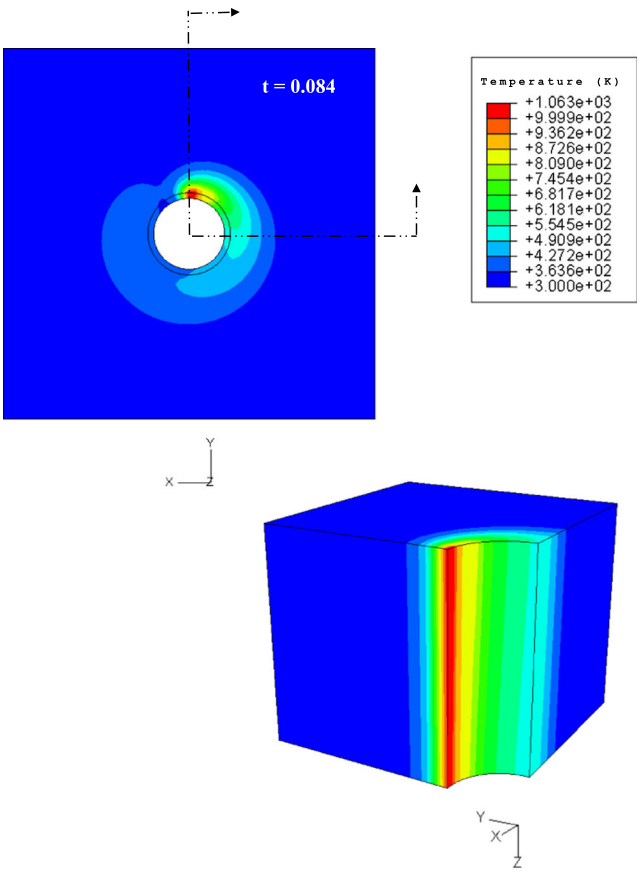

Fig. 4 Temperature contours in the workpiece material at the cooling cycle initiation (t=0.084 s

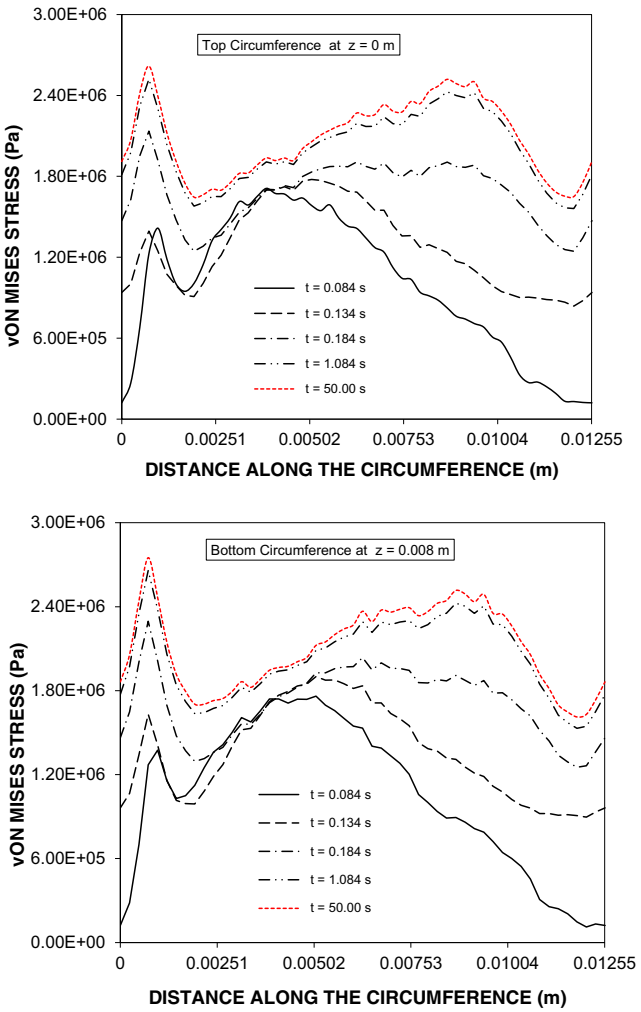

Fig. 5 von Mises stress distribution along the top and bottom circumference of the hole for different cooling periods

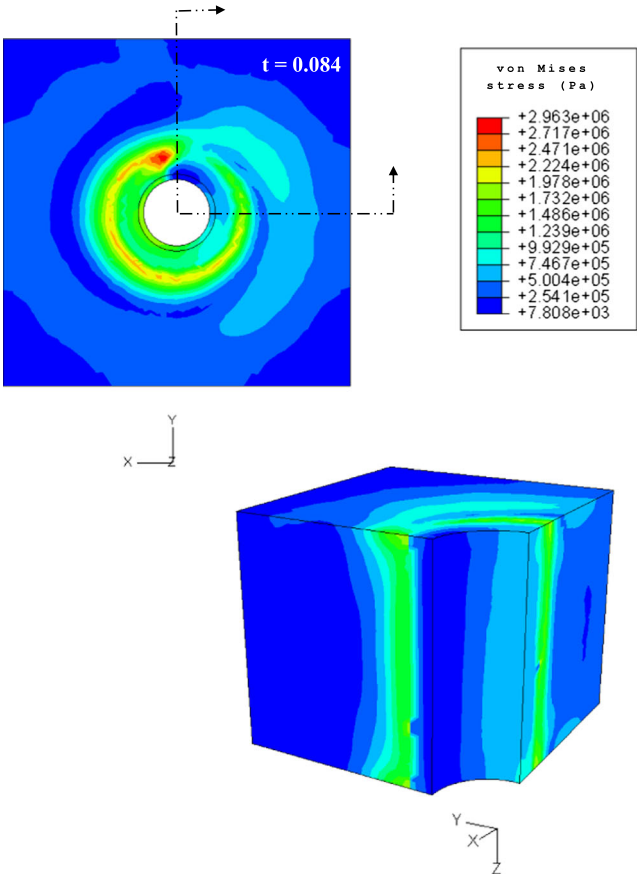

Fig. 6 von Mises stress contours in the workpiece material at the cooling cycle initiation (t=0.084 s)

Morphological changes in the cut section are examined using SEM, EDS, and XRD.

Figure 2 shows temporal variation of temperature predicted from the simulations and obtained from the thermocouple data at 0.5 mm away from the location no. 3 as shown in Fig. 1. It can be observed that temperature predicted agrees well with the thermocouple data. The discrepancies between both results are small, i.e., within the experimental error.

Figure 3 shows temperature distribution at the top and the bottom circumferences of the hole for different cooling periods while Fig. 4 shows temperature contours in the workpiece. The cooling period is initiated at t=0.084 s when the laser beam is switched off after the cutting completion. Temperature remains high at the location where the laser beam is switched off. Temperature decays sharply in the neighborhood of the high-temperature region. The maximum temperature exceeds the melting temperature of aluminum in which case, the superheating in the liquid phase takes place in the melted edge of the cut section. The formation of mushy zone, where temperature varies between the solidus and liquidus temperatures, is observed at around 0.0116≤circumference≤0.119 along the circumference. As the cooling period progresses, temperature around the hole circumference reduces sharply. This situation is also true in the region where superheating of the liquid phase occurs. This sharp reduction in temperature profiles is associated with convective and conduction cooling of the cut surface. It should be noted that convective boundary conditions are incorporated to account for the assisting gas cooling effect. When comparing the distribution of temperature at the top and the bottom circumferences, the behavior of temperature distribution is almost the same at both circumferences for all cooling periods. However, the maximum temperature is higher at the top circumference than that at the bottom circumference. This is attributed to the laser intensity, which is

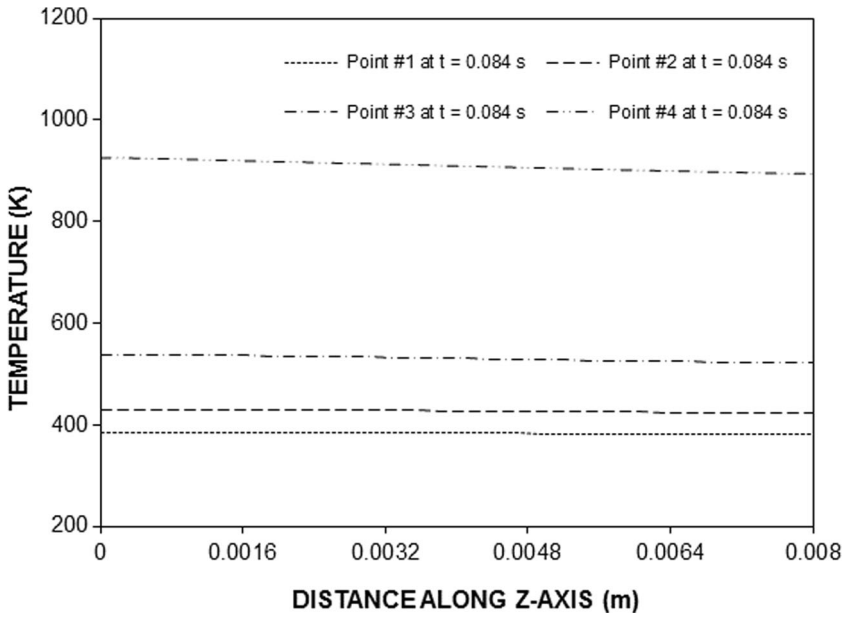

Fig. 7 Temperature distribution along the z-axis at different locations around the hole circumference at the cooling cycle initiation (t=0.084 s)

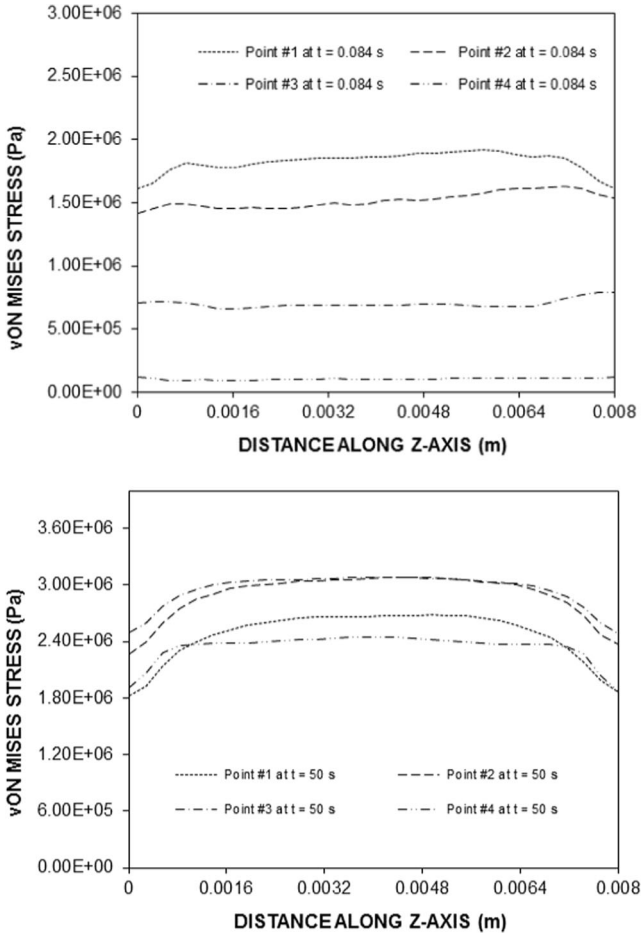

Fig. 8 von Mises distribution along the *z*-axis at different locations around the hole circumference for two cooling periods

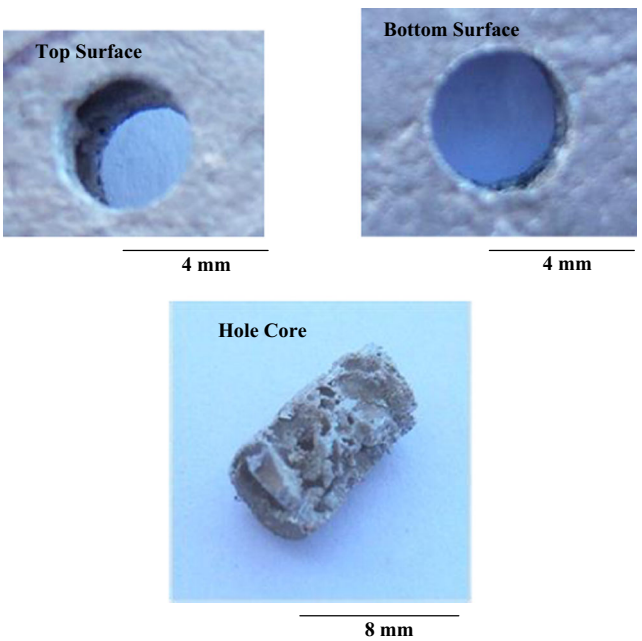

Fig. 9 Photograph of top and bottom surfaces of hole and hole core

higher at the top surface, and it becomes less at the bottom edge due to absorption (Eq. 3).

Figure 5 shows von Mises stress distribution along the top and bottom circumferences of the hole for different cooling periods similar to those shown in Fig. 3 while Fig. 6 shows von Mises stress contours in the workpiece. von Mises stress attains higher values in the vicinity of high-temperature region where the temperature gradient is high. However, in the early cooling periods, von Mises stress attains low values where temperature is high. This behavior is associated with the temperature-dependent elastic modulus, which reduces with increasing temperature (Table 1). As the cooling period progresses, temperature reduces while the rate of thermal strain remains high. In this case, elastic modulus increases, and hence, von Mises stress increases with progressing time. This is more pronounced toward the end of cooling cycle. The high stress regions are also evident in the late cooling periods, and

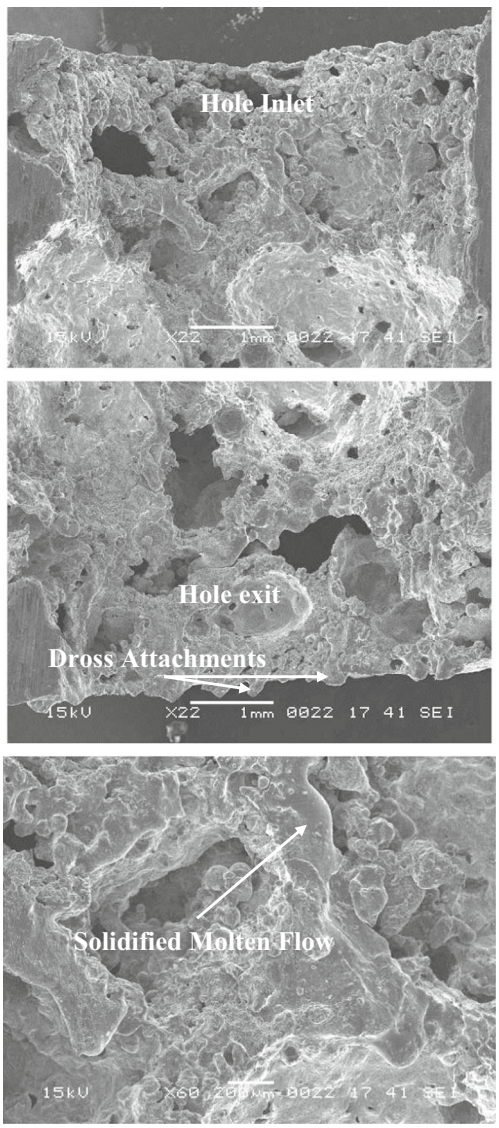

Fig. 10 SEM micrographs of hole surface

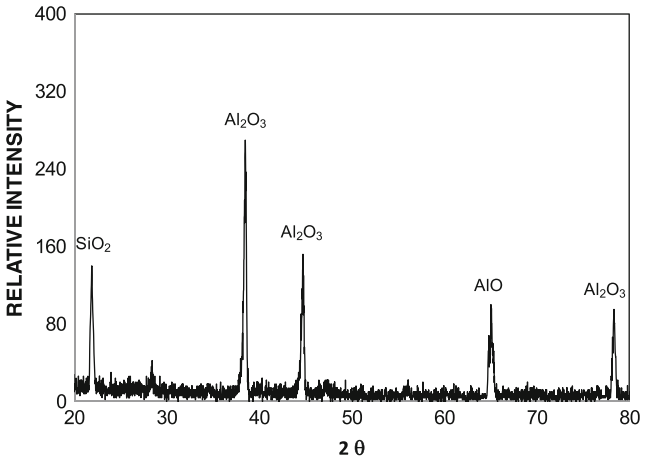

Fig. 11 XRD diffractogram of cut surface

their location moves away from the location of maximum temperature with progressing cooling cycle. The maximum von Mises stress is on the order of 2.4 MPa. The stress behavior is similar for both top and bottom circumferences of the cut section. Although the maximum temperature is slightly different along the top and bottom circumferences, the maximum von Mises stress remains almost the same at both circumferences.

Figure 7 shows temperature distribution along the z-axis at different locations around the circumference for two cooling periods. The locations around the circumference are shown in Fig. 1. z=0 represents the top surface and z=0.008 m corresponds to the bottom surface of the cut section. Temperature variation is almost linear along the cut surface, provided that temperature at the top surface is slightly higher than the bottom surface at the initiation of the cooling cycle (t=0.18 s). Temperature at different locations around the circumference changes according to the last position of the laser beam immediately before switching off the laser power. In this case, temperature remains high along the z-axis at location 4. Once the cooling cycle progresses further (t=200 s), temperature reduces considerably, and temperature difference between the front and back surface becomes negligibly small. It should be noted that the homogenous properties are assumed in the simulations; therefore, the variation of properties due to the structural changes in the foam is neglected due to the simplicity.

Figure 8 shows von Mises stress distribution along the z-axis at different locations around the circumference for two cooling periods. von Mises stress attains lower values in the region of z=0 and z=0.008 m. These regions correspond to top and bottom surfaces of the cut section. In this case, workpiece material expands freely at the top and bottom surfaces while reducing the thermal strain in this region. This, in turn, lowers von Mises stress in this region. However, in the region of at mid-thickness (z=0.004 m), thermal contraction results in development of high thermal strain in this region. This causes attainment of high stress levels in this region. Moreover, von Mises stress corresponding to different locations around the circumference varies; in which case, von Mises stress at location no. 4 becomes less than those at other locations for cooling period t=50 s. This is attributed to the last location of the laser beam where it is ceased off. Consequently, slow cooling rate is resulted at this last location (no. 4) of the laser beam causing the self-annealing effect in the cut section while lowering the stress level in this region.

Figure 9 shows photograph of laser cut hole and its cross section as well as the remaining hole core (slug). It is evident that the hole circumference corresponding to top and bottom surfaces is free from excessive burrs and sideway burnings. In addition, striation patterns are visible at the cut edges and parallel sided holes are cut. Figure 10 shows SEM micrographs of cut surfaces of the hole and the hole core. The cutting results in smooth surfaces at the solid aluminum part of the foam. Since the assisting gas of nitrogen at high pressure is used in the cutting section, molten flow of aluminum is evident around the cut surface. This is attributed to the drag

Table 3 EDS data for elemental composition at the cut surface

Spectrum	O	Si	Al
Spectrum 1	5.9	14.7	Balance
Spectrum 2	0.00	20.5	Balance
Spectrum 3	2.9	9.5	Balance
Spectrum 4	7.5	17.4	Balance

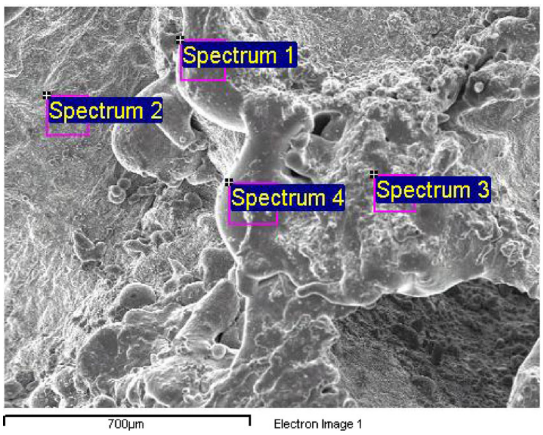

force, due to assisting gas pressure, generated at the molten surface. Moreover, air is trapped in the large size pores in the workpiece prior to cutting. Once the cutting is initiated, the air trapped in the large pores undergoes an exothermic reaction at the molten surface despite the use of high-pressure nitrogen-assisting gas during the cutting process. This is evident from the XRD diffractogram in which aluminum oxide peaks are visible. This is shown in Fig. 11. The presence of AlO peak indicates the formation of single oxide at the cut surface. This is attributed to the presence of less amount of oxygen in the cutting section due to the purging effect of the assisting gas in the cut section. The presence of oxygen is also evident from the EDS data, which is given in Table 3. The close examination of SEM micrographs reveals that top and bottom surfaces of the hole cut section are free from striation patterns at the hole inlet. However, some small locally distributed dross attachments are observed at the hole exit section. The dross attachment is associated with molten flow at the hole exit region. In addition, the assisting gas losses its pressure within the kerf width during the cutting process because of extremely small kerf width size. This causes less drag force acting onto the molten flow. Consequently, liquid metal at the hole exit could not be totally blown away from the kerf side by the assisting gas. The high cooling rate at the hole exit causes the solidification of molten flow in this region, which appears as dross attachment at the hole exit region.

5 Conclusion

Laser cutting of small diameter hole into aluminum foam is carried out. Temperature and stress fields developed in the cutting section are examined numerically using ABAQUS finite element code. The geometric features of the cut section are examined using SEM and optical microscope. The chemical compounds formed at the cut surface are analyzed through XRD and EDS. It is found that temperature exceeds the liquidus temperature of the substrate material around the circumference of the cut section causing superheating of the liquid phase. This, in turn, results in slow cooling of the cut edges while generating annealing effect suppressing the stress levels in the hole circumference. This is more pronounced at location where laser beam power is switched off. von Mises stress attains high values in the region where temperature gradient is high, and it reduces in the high-temperature regions. This behavior is attributed to temperature-dependent elastic modulus of the substrate material which reduces with increasing temperature. It is evident from the cutting experiment that parallel sided holes with no sideways burning can be produced. In addition, no major large burrs are formed around the hole circumference at the hole exit section. SEM micrograph of hole surfaces reveals that no out-off-flatness and striation pattern at the kerf surface are formed. Due to air traps in the large pores, high-temperature oxidation reaction takes place despite the presence of high-pressure nitrogen-assisting gas in the cutting section. The oxidation reactions result in the formation of Al_2O_3 and AlO compounds at the molten surface in the cut section. The molten flow toward the hole exit results in small dross attachment at the cut edge. This is attributed to high convection cooling at the hole exit and reducing assisting gas pressure toward the hole exit causing less drag force acting onto the surface of the molten flow.

Acknowledgments The authors acknowledge the support of King Fahd University of Petroleum and Minerals, Dhahran, Saudi Arabia, for this work.

References

1. Latham WP, Kar A (2000) Review of the simple model for metal cutting with the chemical oxygen-iodine laser, conference: high-power lasers in Civil Engineering and Architecture (CEA), November 1–3, 1999. Proc SPIE - Int Soc Opt Eng 3887:205–210
2. Dubey AK, Yadava V (2008) Laser beam machining—a review. Int J Mach Tools Manuf 48(6):609–628
3. Carter A, Li E (2006) Recent progress in high-power fiber lasers for high-power and high-quality material processing applications, Conference: Advanced Laser Technologies 2005, September 3–6, 2005. Proc SPIE - Int Soc Opt Eng 6344 I
4. Mukarami T, Tsumura T, Ikeda T, Nakajima H, Nakata K (2007) Ansitropic fusion profile and joint strength of lotus-type porous magnesium by laser welding. Mater Sci Eng A 456:278–285
5. Guglielmotti A, Quadrini F, Squeo EA, Tagliaferri V (2009) Laser bending of aluminum foam sandwich panels. Adv Eng Mater 11(11): 902–906
6. Kathuria YP (2003) A preliminary study on laser assisted aluminum foaming. J Mater Sci 38(13):2875–2881
7. Rangari VK, Jeelani MI, Zhou Y, Jeelani S (2008) Fabrication and characterization of MWCNT/thermoplastic microsphere nanocomposite foams. Int J Nanosci 7(2–3):161–169
8. Carcel B, Carcel AC, Perez I, Fernandez E, Barreda A, Sampedro J, Ramos JA (2009) Manufacture of metal foam layers by laser metal deposition. Proc SPIE - Int Soc Opt Eng 7131
9. Chaurasia S, Tripathi S, Munda DS, Mishra G, Murali CG, Gupta NK, Dhareshwar LJ, Rossall AK, Tallents GJ, Singh R, Kohli DK, Khardekar RK (2010) Laser interaction with low-density carbon foam. Pramana J Phys 75(6):1191–1196
10. Yoshida Y, Yajima H, Hashidate Y, Ogura H, Ueda S (2002) Hole drilling of glass-foam substrates with laser. Proc SPIE - Int Soc Opt Eng 4426:154–157
11. Fujimura T, Norimatsu T, Nakai M, Nagai K, Iwamoto A, Mima K (2007) Laser machining of RF foam by second harmonics of Nd:YAG laser. Fusion Sci Technol 51(4): 677–681
12. Yilbas BS, Akhtar SS, Karatas C (2011) Laser trepanning of a small diameter hole in titanium alloy: temperature and stress fields. J Mater Process Technol 211(7):1296–1304
13. Coquard R, Baillis D (2009) Numerical investigation of conductive heat transfer in high-porosity foams. Acta Mater 57: 5466–5479

14. Shuja SZ, Yilbas BS (2000) The influence of gas jet velocity in laser heating-a moving workpiece case. Proc Inst Mech Eng Part C: J Mech Eng Sci 214:1059–1078
15. ABAQUS Theory Manual, Version 6.2, ABAQUS Inc., Pawtucket, USA
16. Bluhm J, de Boer R (1996) Effective stress—a clarification. Arch Appl Mech 66:479–492
17. de Boer R, Ehlers W (1990) The development of the concept of effective stress. Acta Mech 88:77–92
18. Ehlers W, Droste A (1990) A continuum model for highly porous aluminum foam. Tech Mech 19:341–350
19. Deshpande VS, Fleck NA (2000) High strain rate compressive behaviour of aluminium alloy foams. Int J Impact Eng 24: 277–298
20. Yilbas BS, Davies R, Gorur A, Yilbas Z, Begh F, Kalkat M, Akcakoyun N (1990) Study into the measurement and prediction of penetration time during CO_2 laser cutting process. Proc Inst Mech Eng Part B 204:105–113